

Research Article

A Green Synthesis of Ru Modified g-C₃N₄ Nanosheets for Enhanced Photocatalytic Ammonia Synthesis

Derek Hao ¹, Jiawei Ren ¹, Ying Wang ², Hamidreza Arandiyani ^{3,4},
Magnus Garbrecht ⁵, Xiaojuan Bai ⁶, Ho Kyong Shon,¹ Wei Wei,¹ and Bing-Jie Ni ¹

¹Centre for Technology in Water and Wastewater (CTWW), School of Civil and Environmental Engineering, University of Technology Sydney (UTS), Sydney, NSW 2007, Australia

²State Key Laboratory of Rare Earth Resource Utilization, Changchun Institute of Applied Chemistry, Chinese Academy of Sciences, Changchun 130022, China

³Laboratory of Advanced Catalysis for Sustainability, School of Chemistry, The University of Sydney, Sydney 2006, Australia

⁴Centre for Advanced Materials & Industrial Chemistry (CAMIC), School of Science, RMIT University, Melbourne, VIC 3000, Australia

⁵Australian Centre for Microscopy and Microanalysis, The University of Sydney, Sydney 2006, Australia

⁶Beijing Engineering Research Center of Sustainable Urban Sewage System Construction and Risk Control, Beijing University of Civil Engineering and Architecture, Beijing 102612, China

Correspondence should be addressed to Ying Wang; ywang_2012@ciac.ac.cn and Bing-Jie Ni; bingjieni@gmail.com

Received 2 May 2021; Accepted 13 August 2021; Published 6 September 2021

Copyright © 2021 Derek Hao et al. Exclusive Licensee Beijing Institute of Technology Press. Distributed under a Creative Commons Attribution License (CC BY 4.0).

Nitrate is a crucial environmental pollutant, and its risk on ecosystem keeps increasing. Photocatalytic conversion of nitrate to ammonia can simultaneously achieve the commercialization of environmental hazards and recovery of valuable ammonia, which is green and sustainable for the planet. However, due to the thermodynamic and kinetic energy barriers, photocatalytic nitrate reduction usually involves a higher selectivity of the formation of nitrogen that largely limits the ammonia synthesis activity. In this work, we reported a green and facile synthesis of novel metallic ruthenium particle modified graphitic carbon nitride photocatalysts. Compare with bulk graphitic carbon nitride, the optimal sample had 2.93-fold photocatalytic nitrate reduction to ammonia activity (2.627 mg/h/g_{cat}), and the NH₃ selectivity increased from 50.77% to 77.9%. According to the experimental and calculated results, the enhanced photocatalytic performance is attributed to the stronger light absorption, nitrate adsorption, and lower energy barrier for the generation of ammonia. This work may provide a facile way to prepare metal modified photocatalysts to achieve highly efficient nitrate reduction to ammonia.

1. Introduction

Nitrate (NO₃⁻) is a necessary nutrient for plants, whereas high-level of NO₃⁻ enters the food chain via water sources can be toxic and hazardous to the ecosystem [1–3]. The main culprits of NO₃⁻ pollution include agricultural runoff, fertilizer abuse, septic systems, industrial plants, and irrigation systems [4]. Currently, NO₃⁻ contamination has been a serious environmental concern as it can affect the quality of groundwater and surface water, causing health problems to humans [5, 6]. In an oxygen-deficient environment, such as in the digestive tract, NO₃⁻ can be reduced to more toxic nitrite [7, 8]. Nitrite can oxidize low ferritin into methemo-

globin in the human body, causing the loss of oxygen transportation. It can also react with secondary amine compounds to produce carcinogenic nitrosamines [9]. Therefore, it is urgent to develop a novel strategy to remove NO₃⁻ pollution with high efficiency and selectivity.

Ammonia (NH₃) is an important industrial ingredient widely used in fertilizers, pharmaceutical industries, and other areas [10–12]. More importantly, it is also an essential energy source. The decomposition of ammonia is a low-cost and facile process; therefore, using ammonia as a hydrogen carrier is able to solve the hydrogen storage problem to a certain extent [13, 14]. With the increase of the global population, the demand for NH₃ keeps increasing. Currently,

NH₃ is mainly produced via the Haber process, in which gaseous nitrogen (N₂) and water gas are converted to NH₃ under high temperature and high pressure with the assist of catalysts [15]. Every year, the synthesis of NH₃ consumes about 2% of global energy, leading to serious carbon dioxide emission [16–18]. Thus, it is urgent to develop a green synthesis of NH₃ under ambient conditions.

In recent years, photocatalytic synthesis of NH₃ has become a hot research frontier, where researchers are mainly focusing on the reduction of gaseous nitrogen [19–22]. However, the research is still limited in the laboratory, because the strong bond energy of N≡N bonds and the poor solubility of N₂ make the catalytic NH₃ yield efficiency low [16]. Compared with N₂, the required energy for the cleavage of N=O is only 21.68% as that of N≡N bonds. In addition, the solubility of NO₃⁻ is 40000 times higher than that of N₂ [23]. Therefore, if the waste NO₃⁻ can be converted to NH₃, the conversion of environmental hazards to valuable energy resources will be more sustainable for the planet.

Graphitic carbon nitride (g-C₃N₄) is a metal-free photocatalyst, which is a rising star in photocatalysis because it has the advantages of facile synthesis, wide sources, and good photocatalytic activity for redox reactions [24–26]. In recent years, several kinds of g-C₃N₄-based photocatalysts have been prepared and applied in NO₃⁻ wastewater treatment, such as TiO₂/g-C₃N₄ [27], Mn₂O₃/g-C₃N₄ [28], and g-C₃N₄@AgPd heterojunction [29]. However, the main aim is to convert NO₃⁻ to N₂ to reduce environmental hazards. Compared with the generation of N₂, the reduction of NO₃⁻ to NH₃ is more challenging in terms of kinetics and thermodynamics, as it is an eight-electron process with multiple steps [30]. On the other hand, many ruthenium-containing compounds exhibit good catalytic properties because of their unique electronic structure [31–34]. Meanwhile, ruthenium (Ru) can absorb the light in the visible spectrum, and it is being actively researched for solar energy technologies [35, 36]. Nevertheless, toxic reducing agents like ethylene glycol are usually required to reduce Ru³⁺ to Ru⁰, making the synthesis complex, dangerous, and unecofriendly [37]. Until now, Ru modified g-C₃N₄ photocatalysts for highly efficient NO₃⁻ reduction to NH₃ have never been reported, and the reaction mechanism is not clear.

In this work, we report a green synthesis of Ru modified g-C₃N₄ nanosheets with significantly enhanced photocatalytic activity on the reduction of NO₃⁻ to NH₃. Herein, waste green tea bags were used to reduce the Ru³⁺, and the photocatalytic activity of the optimized sample was 2.93-fold as that of bulk g-C₃N₄ under simulated sunlight irradiation. The material preparation process was ecofriendly without using strong reducing reagent. Based on experimental and theoretical studies, the introduction of Ru to g-C₃N₄ can not only boost the light absorption, the adsorption of NO₃⁻, but also accelerate the separation of electron-hole pairs. The thermodynamic energy barrier for the rate determining step in NO₃⁻ reduction to the NH₃ process is calculated to be less than 0.75 eV, which is much lower than the competing H₂ generation (0.98 eV) and N₂ formation (1.36 eV), leading to the preference of generating NH₃. This work provides a novel approach to synthesize metallic

particle-based photocatalysts for highly efficient photocatalytic NO₃⁻ reduction to synthesize NH₃.

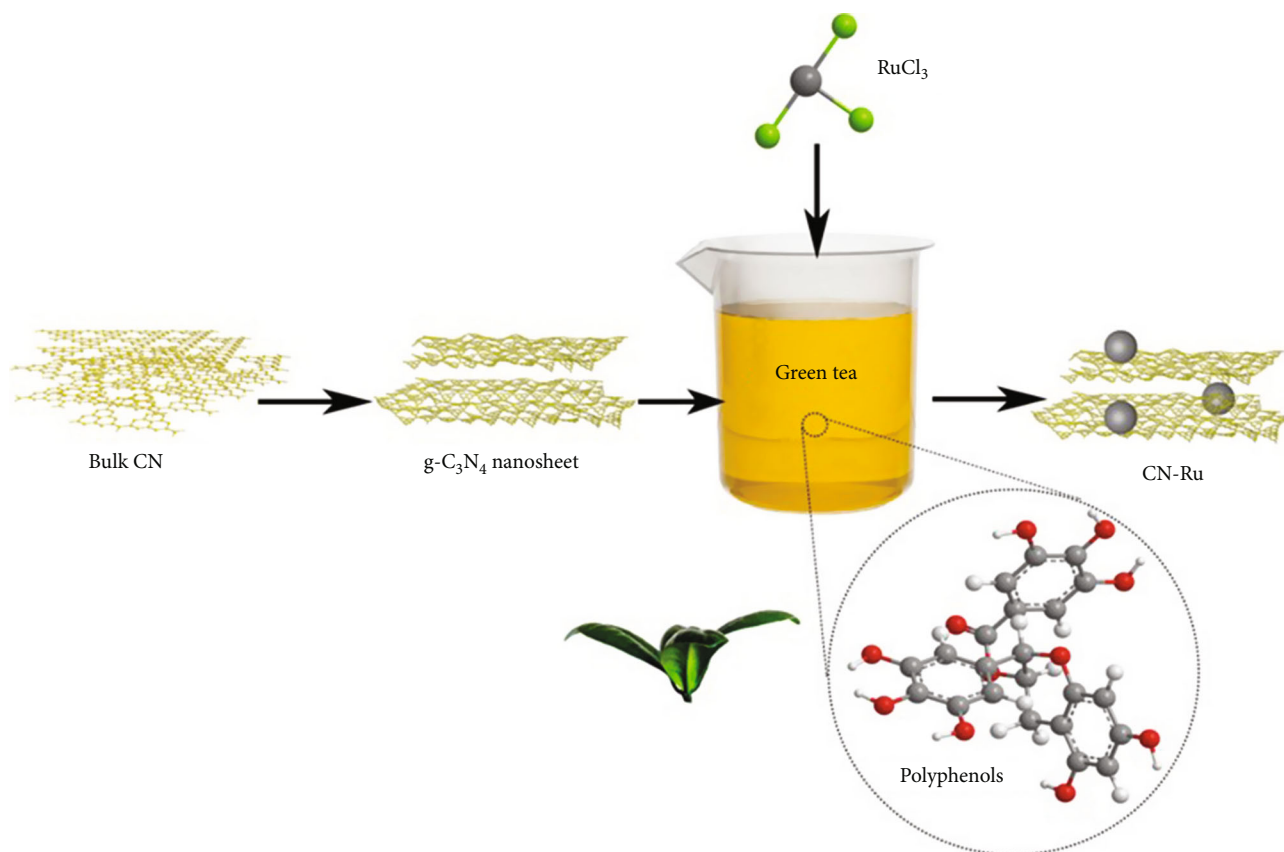
2. Experimental Section

2.1. Chemicals and Synthesis of Materials. All the used chemicals including ruthenium trichloride (RuCl₃), sodium nitrate (NaNO₃), sodium sulfate (Na₂SO₄), dicyandiamide, sulfuric acid (H₂SO₄), formic acid, and dimethyl sulfoxide (DMSO) are analytical reagent and used without further purification. These chemicals were purchased from Merck Australia.

2.2. Synthesis of g-C₃N₄ Nanosheets. g-C₃N₄ was prepared via the thermal polymerization of dicyandiamide. Firstly, 5 g of dicyandiamide was put in a 50 mL corundum crucible without the lid. Then, the crucible was transferred into the oven and heated from 25 to 540°C with the heating rate of 4°C/min. After heating at 540°C for 4 h in air, the bulk g-C₃N₄ was obtained. The g-C₃N₄ nanosheets were synthesized via the ultrasonic peeling of bulk g-C₃N₄ in water. In details, 500 mg of bulk g-C₃N₄ was added in 800 mL water and put under ultrasonic bath for 24 h. Finally, the ultrathin g-C₃N₄ nanosheets were successfully obtained and named as 2D-CN.

2.3. Synthesis of Ru/g-C₃N₄. Herein, we used waste green tea as the reduction reagent to prepare Ru modified g-C₃N₄ (Scheme 1). To get simulated waste tea bags, 5 tea bags were put in boiled water for 20 min. Then, the 5 used tea bags were put in 500 mL and boiled for 30 min. After that, the tea water was gone through a filter for further use. A certain amount of RuCl₃ and 0.5 g of g-C₃N₄ nanosheets was put into 150 mL prepared tea water and under magnetic stir for 24 h. Finally, the powder was washed by water and ethanol for 5 times and then dried at 60°C for 4 h. The amounts of RuCl₃ used were 0.005, 0.01 and 0.038 g, and the obtained samples were named as CN-Ru-0.5, CN-Ru-1, and CN-Ru-3, respectively.

2.4. Characterizations. The X-ray diffraction (XRD) patterns of the samples were tested with a Bruker D8 Discover XRD with intense Cu K α radiation (40 kV and 40 mA, λ = 1.5406 Å) at room temperature. The morphology observation on the materials was carried out using a Zeiss Supra 55VP scanning electron microscope (SEM), with an operating voltage of 5–15 kV. The images of SEM-energy-dispersive X-ray spectroscopy (EDS) for elemental mapping were obtained with the Oxford Ultim Max. High-angle annular dark-field scanning transmission electron microscopy (HAADF-STEM) and EDS mapping were performed on a double-corrected FEI Themis-Z 60–300 transmission electron microscopy (TEM) equipped with ChemiSTEM EDS detector system for ultra-high count rates. The X-ray photoelectron spectra (XPS) of the samples were tested with a Thermo Fisher Scientific K-Alpha+X-ray photoelectron spectroscopy. The UV-vis diffuse reflectance spectra (DRS) of prepared samples were obtained from a Perkin Elmer Lambda 950 UV/VIS/NIR spectrometer, using high-purity



SCHEME 1: Schematic illustration of the preparation of Ru modified g-C₃N₄ nanosheets.

barium sulfate (BaSO₄) as the blank reference. Photoluminescence (PL) spectra were obtained from a Shimadzu RF-6000 fluorescence spectrometer excited at 325 nm. The photocurrent, electrochemical impedance spectroscopy (EIS) and Mott-Schottky curves of the samples were obtained from an electrochemical working station (CHI-760E) in 0.1 M Na₂SO₄ solution (details shown in supplementary materials).

2.5. Photocatalytic Activity Testing. The photocatalytic nitrate reduction performance was carried out with a self-made quartz reactor under simulated sunlight irradiation. During the reaction process, the light intensity was 600 mW/cm² (HSX-F300), and it was measured by a radiometer. The distance between the light and the reactor was 10 cm. Firstly, 20 mg of the samples was weighed and put into the reactor. Then, 95 mL of NaNO₃ (10 mg/L) solution and 5 mL of formic acid (200 μL/L) were added. Before the reaction, argon was purged into the solution to remove air. After 2 h strong stir to make the powder catalysts uniformly dispersed in the solution, the light was turned on and the light irradiation lasted 4 h. In each hour, 3 mL of liquid was sampled from the reactor. The concentration of ammonium was measured by UV-vis spectrometer using Nessler's reagent method and was further verified by 1H-Nuclear magnetic resonance spectroscopy (NMR) analysis. The concentration of NO₃⁻ and NO₂⁻ was measured by a high-

pressure integrated capillary anion chromatography (IC). The exact details of Nessler's reagent method, NMR, and IC are shown in the supplementary materials (Figure S1-S4).

2.6. Density Functional Calculation. The calculations of geometry structures and energies were carried out by density functional theory (DFT) with Vienna ab initio simulation package (VASP) [38–41]. The exact details are presented in supplementary materials.

3. Results and Discussion

3.1. Structure and Morphology. In the XRD patterns of g-C₃N₄ (Figure S5 in supporting information, SI), two distinct peaks at 13.1 and 27.1° can be assigned to the (100) and (002) crystal plane diffraction (JCPDS 87-1526) [42]. After peeled off by ultrasonic powder, the peak intensity decreased, indicating the reduced crystallinity. Since the loaded amount of Ru is not high, it cannot be detected by XRD. Then, HRTEM and SEM were used to explore the morphology of the prepared samples. As shown in Figure 1(a), the g-C₃N₄ nanosheets showed an ultrathin film layer structure. The CN-Ru-1 sample had the same morphology as 2D-CN with Ru particles loaded on the g-C₃N₄ nanosheets (dark spots in Figure 1(b)). The size of the Ru particles was less than 5 nm. To further investigate the lattice, the Ru particles were zoomed in and displayed in Figure 1(c). The lattice distance of 0.234 nm

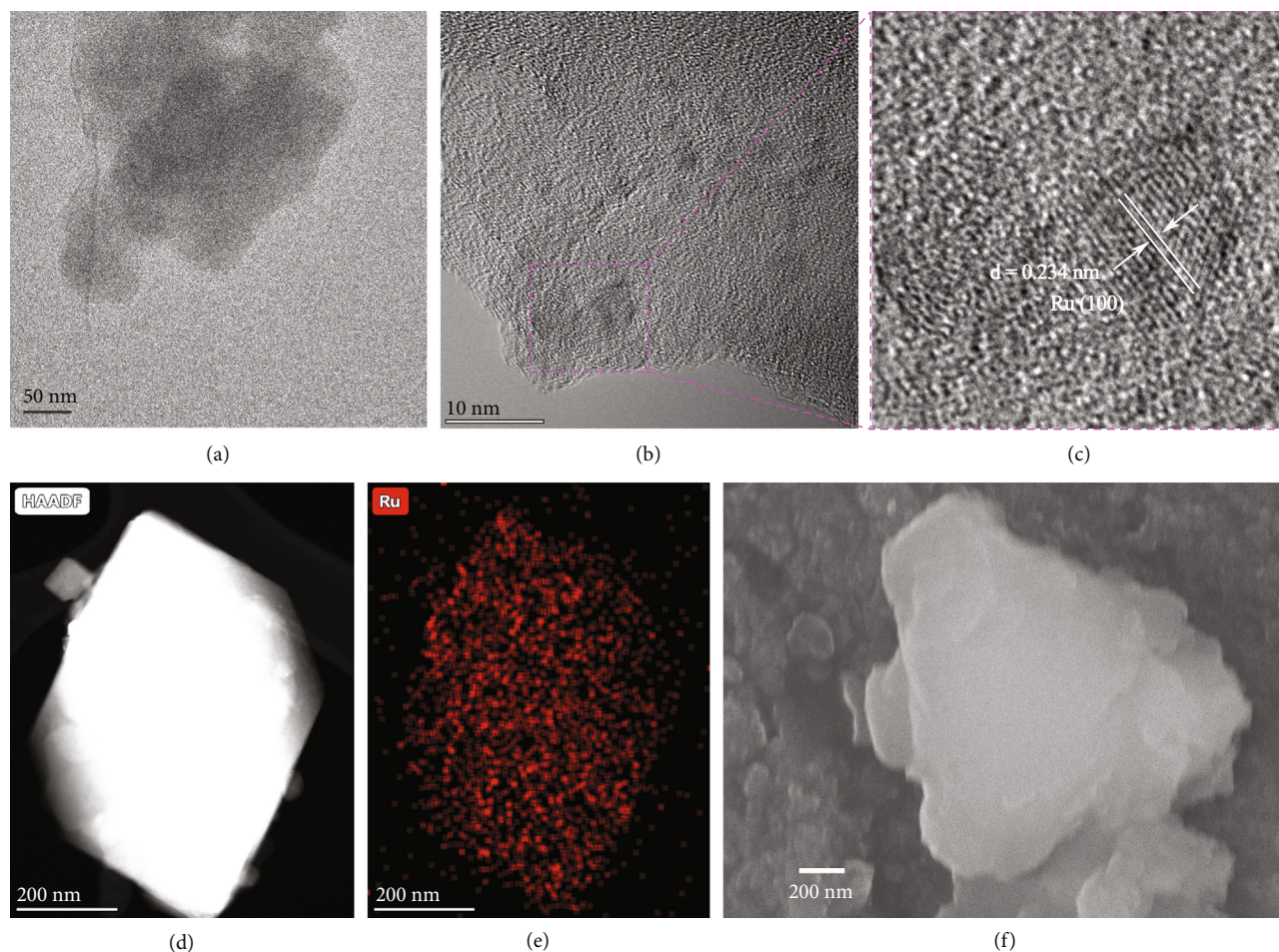


FIGURE 1: HRTEM image of g-C₃N₄ nanosheets (a), CN-Ru-1 (b) and the zoom-in part of the lattice (c), high-angle annular dark-field image (d), energy dispersive spectroscopy for Ru element mapping (e), and SEM image of CN-Ru-1 (f).

can be indexed to the (100) of metallic Ru. Additionally, the high-angle annular dark-field (HAADF) image and energy dispersive spectroscopy (EDS) for Ru element mapping were obtained to further confirm the component of the CN-Ru sample. As exhibited in Figures 1(d) and 1(e) and Figure S6, Ru particles are uniformly distributed on g-C₃N₄ nanosheets. SEM image was also employed to study the morphology of CN-Ru-1 (Figure 1(f)). In the SEM image, we can only see the nanosheet structure of g-C₃N₄, since the size of Ru particles was too small to be observed by SEM.

Then, XPS was used to study the components of the prepared samples. Figures 2(a) and 2(b) are the narrow C 1s spectra of 2D-CN and CN-Ru-1. The three peaks of 2D-CN at 293.6, 287.9, and 284.6 eV can be assigned to the conjugated π electrons and sp²-hybridized C and C-C bonds [10]. Compared with 2D-CN, two new peaks appeared in the narrow XPS spectra of C of CN-Ru-1. The peak at 286.1 eV was attributed to C-O which came from the green tea (Figure 2(b)) [43]. The other new peak at 280.2 eV is associated with Ru⁰ [44]. Both 2D-CN and CN-Ru-1 have 3 peaks in the narrow N 1s spectra. In Figure 2(c), the three peaks at 404.4, 400.0, and 398.4 eV of 2D-CN are attributed to the charging effect, tertiary nitrogen, and sp²-hybridized nitrogen. Notably, the three peaks of N of CN-Ru-1 shifted to

404.9, 400.1, and 398.6 eV, which was caused by the interaction between 2D-CN and Ru [45].

Based on the XRD, SEM, TEM, and XPS results, it can be concluded that metallic Ru particle modified g-C₃N₄ nanosheets were successfully fabricated.

3.2. Enhanced Photocatalytic NO₃⁻ Reduction to NH₃. Herein, we used photocatalytic NO₃⁻ reduction to NH₃ to evaluate the catalytic activity of samples. After 4-hour simulate sunlight irradiation, all the samples exhibited apparent photocatalytic activity on the reduction of NO₃⁻ to NH₃ (Figure 3(a)). The NH₃ yield rate of 2D-CN was 1.126 mg/h/g_{cat}, and it was 1.26-fold as that of bulk g-C₃N₄. When metallic Ru was used to modify the 2D-CN, the photocatalytic activity increased remarkably. Among all the samples, CN-Ru-1 was the most active one (2.627 mg/h/g_{cat}), and its activity is 2.93 times higher than bulk g-C₃N₄. Cycle stability is crucial for the study and application of photocatalysts. After the fourth cycle, the NH₃ yield of CN-Ru-1 was still 2.32 mg/h/g_{cat}, which was 88.16% as the fresh catalyst, indicating good cycle stability for reusage. The use of formic acid did not influence of the detection by the accuracy of Nessler's reagent method (Figure S7).

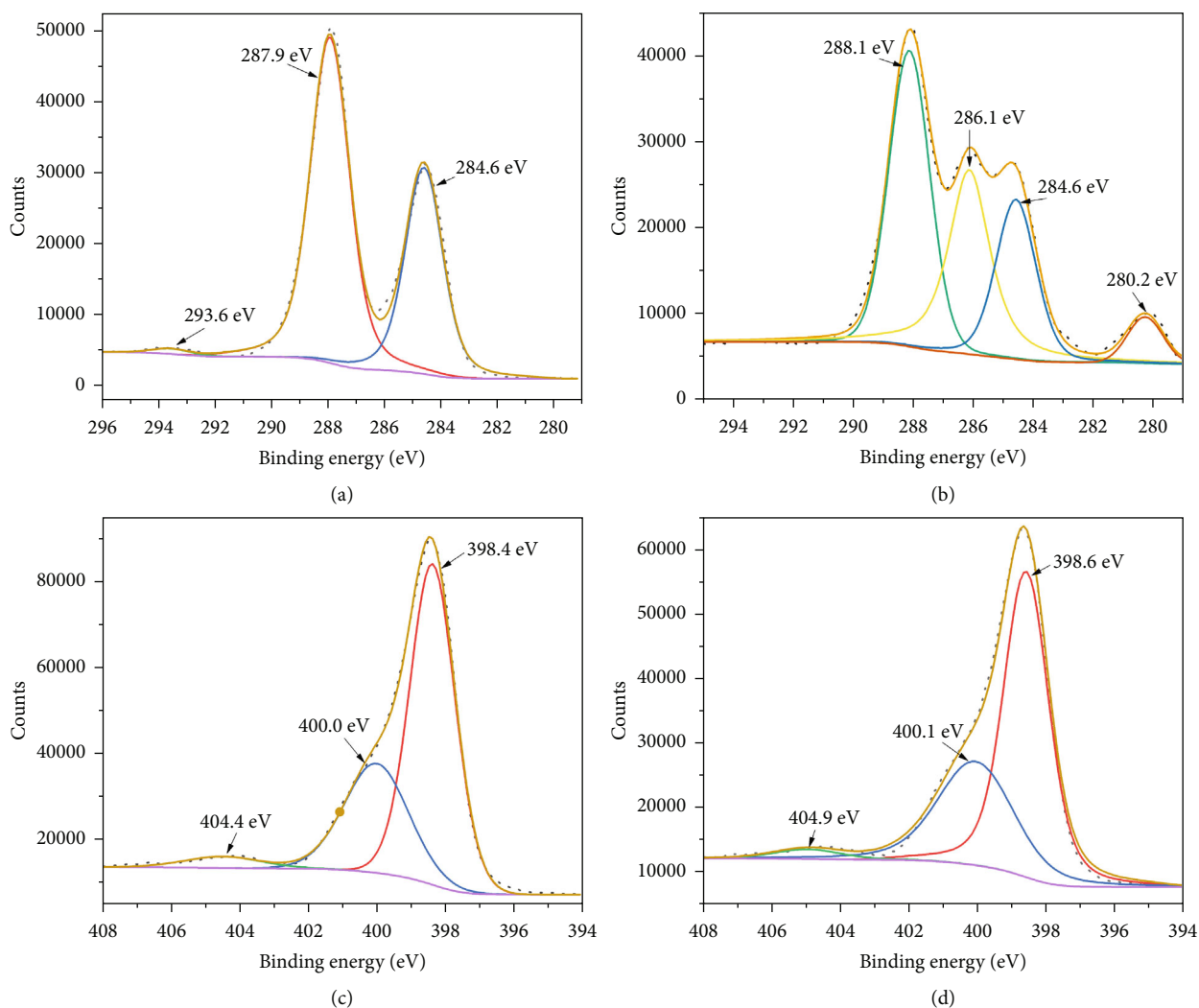


FIGURE 2: Narrow C 1s and Ru 3d XPS spectra of 2D-CN (a) and CN-Ru-1 (b). Narrow N 1s XPS spectra of 2D-CN (c) and CN-Ru-1 (d).

To confirm the source of NH_3 generated, we carried on the ^{15}N isotope experiment with $\text{Na}^{15}\text{NO}_3$. A series of $^{15}\text{NH}_4\text{Cl}$ solutions with different concentration were firstly used to generate a standard line, and then the concentration of photocatalytic reactions can be analyzed. As shown in Figure 3(c), the standard 1H-NMR spectrum of $^{15}\text{NH}_4^+$ had two peaks with a coupling constant of 73.14 Hz. In the solution after photocatalytic reaction of CN-Ru-1 with $^{15}\text{NO}_3^-$, two characteristic $^{15}\text{NH}_3$ peaks were also found, and the calculated concentration of NH_3 was 2.05 mg/L, which well matched the results of UV-vis spectrophotometry. The NMR results can confirm that the formation of NH_3 is attributed to the photocatalytic reduction of NO_3^- .

Besides NH_3 , there might be some other products of the NO_3^- reduction. Herein, we used ion chromatography to measure the concentration of NO_3^- and NO_2^- . After 4 h light irradiation, bulk CN reduced 48.85% of the NO_3^- (10 mg/L), 50.77% of which was converted to NH_3 . Under the same condition, CN-Ru-1 eliminated 92.85% of NO_3^- , and the NH_3 selectivity was 77.9%. The UV-vis spectrophotometry, 1H-NMR, and ion chromatography results confirmed that

both the NO_3^- conversion rate and NH_3 selectivity were significantly increased by CN-Ru-1, compared with bulk CN.

In Table S1, we summarized several typical g- C_3N_4 , TiO_2 , and other materials for photocatalytic NO_3^- reduction in literature for comparison. Many materials can achieve highly efficient NO_3^- removal, whereas the ammonia selectivity is quite low. Pd/ TiO_2 can get a high NH_3 selectivity of 76.9%, but its catalytic activity is really poor [46]. Nevertheless, the CN-Ru-1 reported in this work can simultaneously realize both high NO_3^- removal and high NH_3 selectivity.

3.3. Mechanism of the Enhanced Performance. Light absorption is an essential step for photocatalytic reaction. Figure 4(a) shows the UV-vis DRS of bulk CN, 2D-CN, and CN-Ru samples. The absorption edge of bulk CN was at about 460 nm, indicating a bandgap of 2.70 eV. When bulk CN was converted to 2D-CN, the absorption edge had a blue shift to 430 nm, with a wider bandgap of 2.88 eV. When the 2D-CN was modified by metallic Ru particles, the absorption edge showed a redshift. Meanwhile, the light absorption in the visible light region was also

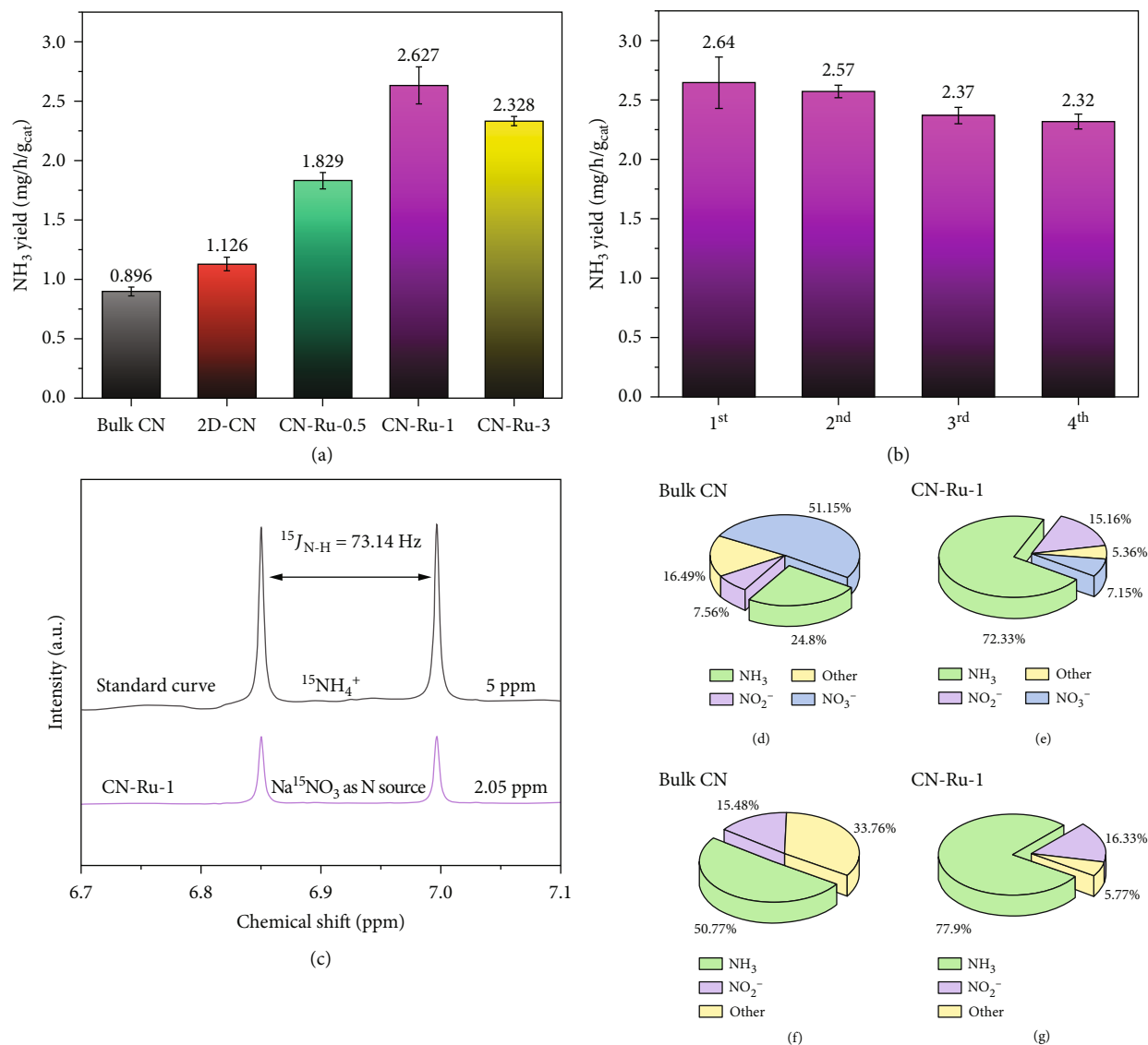


FIGURE 3: (a) Photocatalytic activity of bulk CN, 2D-CN, and CN-Ru samples and (b) cycle stability of CN-Ru-1. (c) The NMR spectra of $^{15}NH_4Cl$ standard solution and the final photoreduction production of $Na^{15}NO_3$ by CN-Ru-1. The proportions of productions and NO_3^- after photocatalytic reaction by (d) bulk CN and (e) CN-Ru-1. The selectivity of photocatalytic reduction of NO_3^- by (f) bulk CN and (g) CN-Ru-1.

significantly enhanced. The increased light absorption enabled to make the catalysts absorb more photons, boosting the solar energy utilization ratio. The density of states of $g-C_3N_4$ and CN-Ru is calculated by DFT (Figure 4(b)). Compared with $g-C_3N_4$, the introduction of metallic Ru can bring some metallicity to the composite catalysts, which is beneficial to the transfer and separation of photocatalytic generated electron-hole pairs [47].

In order to explore more direct evidence about the transfer and separation of photogenerated electron-hole pairs, the photocurrent response, EIS, and PL spectra of bulk CN, 2D-CN, and CN-Ru samples were tested. Figure 4(c) is the photocurrent response image. All the tested samples had apparent and rapid photocurrent response under light irradiation. Among all the samples, the photocurrent intensity of CN-Ru-1 was the strongest, which followed the same

trend as the photocatalytic activity, indicating that CN-Ru-1 had the fastest separation and transfer of electrons and holes. The photocurrent slightly decreased in 200 s, which was caused by the decreased interaction between the powder catalysts and the ITO glass [48]. It does not mean the photocatalysts have poor stability. In the EIS Nyquist plot, the bulk CN had the largest arc radius because of its poor conductivity. The 2D-CN got a smaller arc radius as it had better conductivity than bulk CN. When the 2D-CN got modified by metallic Ru, the arc radius of the EIS Nyquist plot significantly decreased, because Ru had strong conductivity. The more metallic Ru loaded, the better conductivity the sample got. The PL spectra of bulk CN, 2D-CN, and CN-Ru samples were displayed in Figures 4(e) and 4(f). Bulk CN showed a broad and strong emission spectrum with profiles slightly deviating from a perfect Guanine curve centered at about

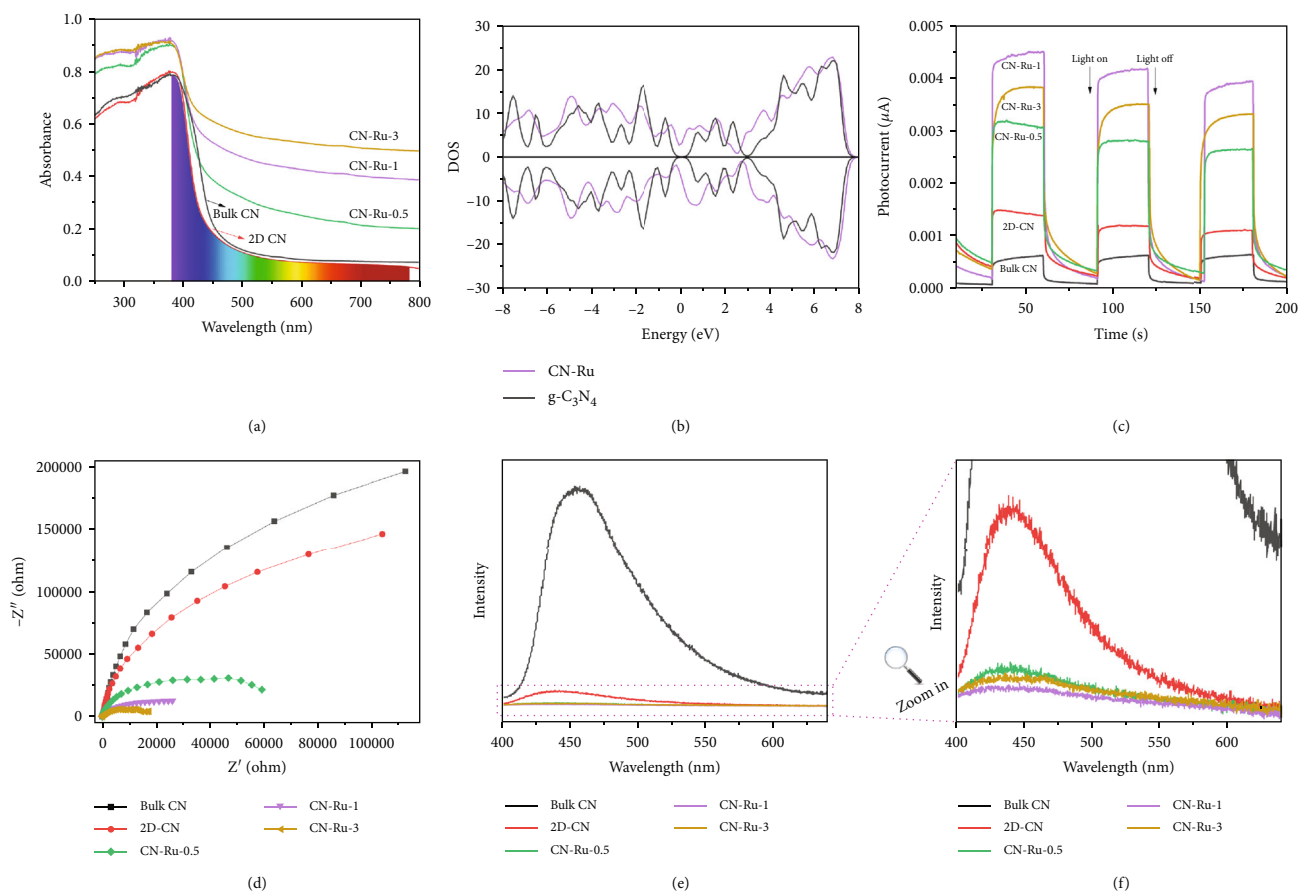


FIGURE 4: UV-vis DRS of bulk CN, 2D-CN, and CN-Ru samples (a). Density of states of g-C₃N₄ and CN-Ru (b). Photocurrent response (c), EIS (d), and PL spectra (e, f) of bulk CN, 2D-CN and CN-Ru samples.

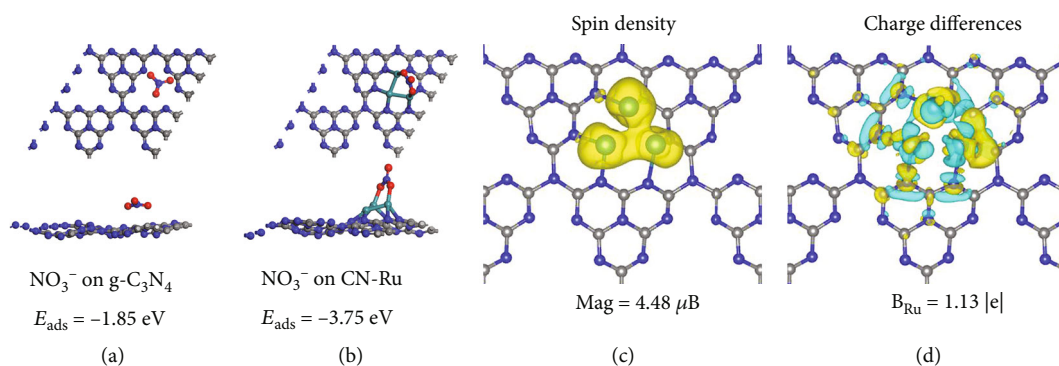


FIGURE 5: Adsorption structures and calculated adsorption energies of NO₃⁻ adsorbed on g-C₃N₄ (a) and CN-Ru (b). Optimized spin density (c) and charge differences (d) of CN-Ru.

460 nm. Compared with bulk CN, the PL intensity of the other samples decreased significantly, which means the recombination of photoinduced charge carriers was obstructed, and it is helpful for the enhanced photocatalytic activity [49].

Experimental studies on NO₃⁻ reduction have shown that Ru modified g-C₃N₄ plays an essential role in improving NH₃ production compared with pure g-C₃N₄. To further understand the reaction mechanism and the origin of high

activity and selectivity of CN-Ru, the density functional theory calculation is performed. NO₃⁻ adsorption, the first step of NO₃⁻ reduction, was first calculated, and the optimized adsorption structures, as well as the adsorption energies, are listed in Figures 5(a) and 5(b). The adsorption energy of NO₃⁻ on g-C₃N₄ was -1.85 eV, and it was -3.75 eV on CN-Ru. It is clearly seen that Ru modification increased the NO₃⁻ stability by 2.03 times compared with

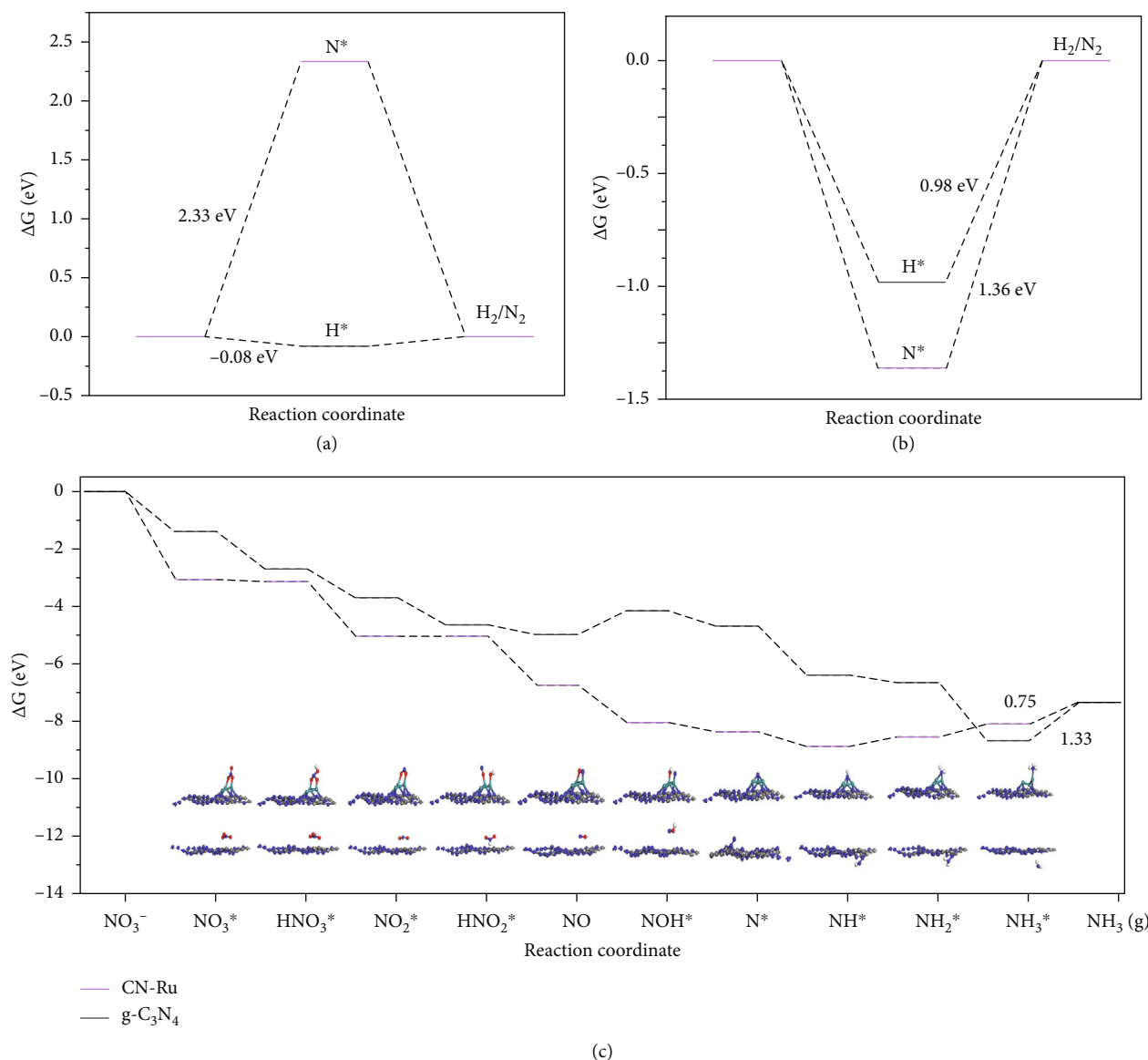


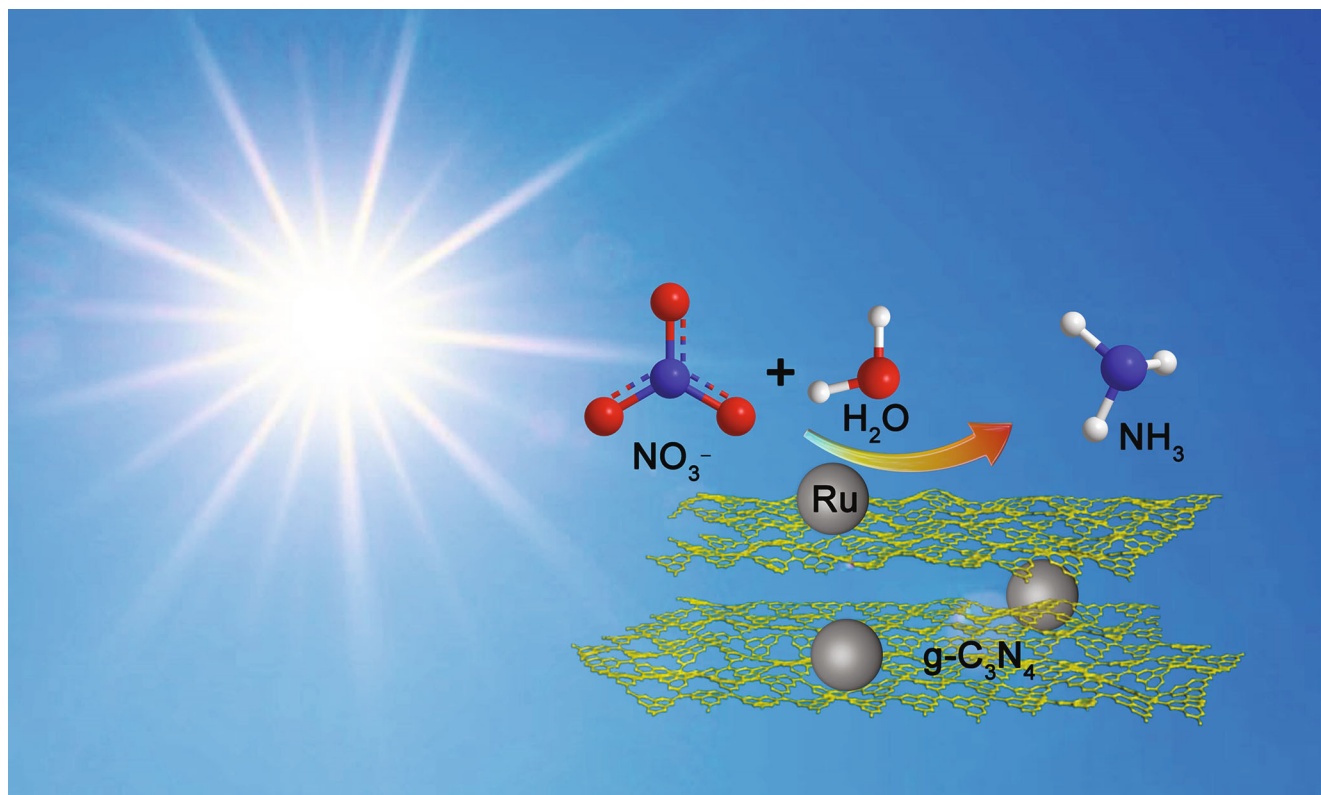
FIGURE 6: Calculated free energy differences between the formation of H_2 and N_2 on $g-C_3N_4$ (a) and CN-Ru (b). Calculated free energy changes of NO_3^- reduction to NH_3 on $g-C_3N_4$ and CN-Ru (c).

pristine $g-C_3N_4$, indicating the following NO_3^- reduction step proceeds more easily, consistent with the experimental observations.

Furthermore, metallic Ru particles involve a high spin density on Ru cluster and positive Bader charge, as well as a zero gap, which can enhance the electron transfer ability (Figures 5(c) and 5(d)). Since Ru cluster got a positive Bader charge, the photocatalytic generated electrons for $g-C_3N_4$ can be accumulated on Ru, making it as the active sites. At the same time, the CN-Ru system got some magnetic properties, and the spin density is concentrated on Ru. All these electronic structure results are responsible for the improved photocatalytic activity of CN-Ru.

To further understand the role of metallic Ru particles in the NO_3^- reduction process, we calculated the free energy diagrams of NO_3^- reduction on $g-C_3N_4$ and CN-Ru. Compared with the generation of NH_3 , there are two main com-

peting reactional products for the photocatalytic reduction of NO_3^- including H_2 and N_2 . For $g-C_3N_4$, it is very easy to take part in hydrogen generation reaction, while the formation of N_2 is very difficult because a higher thermodynamic energy barrier of 2.33 eV should be overcome (Figure 6(a)). As for CN-Ru, the thermodynamic energy barriers of the formation of H_2 and N_2 are 0.98 and 1.36 eV (Figure 6(b)). All free energy curves are downhill from NO_3^- to HNO_2 , and although the reaction pathway is different, the thermodynamic energy barrier for the rate determining step in this process is all calculated to be less than 0.75 eV (Figure 6(c)), which is much lower than those of $2H \rightarrow H_2$ (0.98 eV) and $2N \rightarrow N_2$ (1.36 eV), suggesting that induced Ru cluster played a key role in the enhancement of the photocatalytic activity and selectivity for NO_3^- reduction to form NH_3 , in good agreement with the experimental observations.



SCHEME 2: The scheme for the photocatalytic nitrate reduction to ammonia on the $g\text{-C}_3\text{N}_4/\text{Ru}$ catalysts.

Based on the experimental and calculated results, the mechanism for the enhanced photocatalytic NO_3^- reduction to NH_3 activity can be summarized as follows (Scheme 2). Firstly, the introduction of metallic Ru caused a redshift of the absorption edge as well as broad absorption in visible light range, which boosted the absorption of photons and the utilization of solar light. Secondly, CN-Ru samples have much better conductivity and higher separation efficiency of photogenerated electron-hole pairs than $g\text{-C}_3\text{N}_4$. Thirdly, the high spin density of Ru cluster and its positive Bader charge can accumulate electrons, making the adsorption and cleavage of NO_3^- easier. More importantly, the thermodynamic energy barrier for the rate determining step in this process is all calculated to be less than 0.75 eV (Figure 6(c)), which is much lower than the competing H_2 generation (0.98 eV) and N_2 formation (1.36 eV), leading to the preference of generating NH_3 and higher activity.

Using green tea as reducing reagent to prepare nanomaterials is promising because it is cost-effective. More importantly, the operation and storage are much safer than using strong reducing reagent like sodium borohydride. The tea polyphenols of green tea are regarded as active ingredients to achieve reduction reactions [50, 51]. Meanwhile, the average reduction potential of green tea is about 0.219 V, indicating that the approach reported in this work can be expanded to the synthesis of other metal-based materials [52]. In Figure S8, we summarized the elements that can be reduced to zero valent theoretically, including Tc, Ru, and Cu, which would potentially use the proposed approach [53].

4. Conclusion

In summary, we used a facile and green approach to synthesize novel metallic Ru modified $g\text{-C}_3\text{N}_4$ nanosheets as photocatalysts for enhanced NO_3^- reduction to NH_3 . The optimal sample (CN-Ru-1) had the highest NH_3 yield rate of 2.627 mg/h/g_{cat}, and it was 2.93 times as that of bulk CN. After 4-hour light irradiation, CN-Ru-1 eliminated 92.85% of NO_3^- , and the NH_3 selectivity was 77.9%. After four cycles, the sample still had good photocatalytic performance (88.16% as the fresh catalyst). NMR and ^{15}N isotope labeling provided solid evidence that the N of NH_3 was from the reduction of NO_3^- . The $g\text{-C}_3\text{N}_4$ nanosheets modified by metallic Ru particles have stronger light absorption, better conductivity, and more rapid separation of electron-hole pairs. With the enhanced adsorption energy of NO_3^- and the low thermodynamic energy barriers, the photocatalytic activity and selectivity were increased significantly. The results and findings of this work may provide a new platform for the facile and green synthesis of metal particle modified photocatalysts for reducing NO_3^- to NH_3 under ambient conditions.

Data Availability

The authors declare that the main data supporting the findings in this study are available within the article and its supplementary information. Additional data are available from the corresponding authors upon reasonable request.

Conflicts of Interest

The authors declare no conflict of interest.

Authors' Contributions

D. H., J.R., H.K.S., X.B., and B.J.N. proposed the project and designed the experiment. D.H., J.R., and W.W. prepared the materials and carried out the characterizations. H.A. and M.G. contributed to the TEM characterizations. Y.W. carried out the DFT calculations. The manuscript was written and edited by all the authors. Derek Hao and Jiawei Ren contributed equally to this work.

Acknowledgments

This work is supported by an Australian Research Council (ARC) Future Fellowship (FT160100195), the National Key Research and Development Program of China (2016YFA0602900), the National Natural Science Foundation of China (21673220), Department of Science and Technology of Sichuan Province (2017GZ0051), and Jilin Province Science and Technology Development Program (20190201270JC, 20180101030JC). Part of the computational time is supported by the High Performance Computing Center of Jilin University and Jilin Province, as well as Network and Computing Center of Changchun Institute of Applied Chemistry. Derek Hao acknowledges the technical support of Beijing NBET Technology Co., Ltd. The authors also acknowledge the Sydney Analytical (USYD), CTWW, MAU, and Chem Lab of UTS for the lab supports.

Supplementary Materials

S1: electrochemical characterizations. S2: ¹H-NMR and HPIC. S3: density functional calculation. (*Supplementary Materials*)

References

- [1] F.-J. Yue, S. Waldron, S. L. Li et al., "Land use interacts with changes in catchment hydrology to generate chronic nitrate pollution in karst waters and strong seasonality in excess nitrate export," *Science of the Total Environment*, vol. 696, article 134062, 2019.
- [2] P. F. Swann, "The toxicology of nitrate, nitrite and nitroso compounds," *Journal of the Science of Food and Agriculture*, vol. 26, no. 11, pp. 1761–1770, 1975.
- [3] P. Santamaria, "Nitrate in vegetables: toxicity, content, intake and EC regulation," *Journal of the Science of Food and Agriculture*, vol. 86, no. 1, pp. 10–17, 2006.
- [4] K. Wick, C. Heumesser, and E. Schmid, "Groundwater nitrate contamination: factors and indicators," *Journal of Environmental Management*, vol. 111, pp. 178–186, 2012.
- [5] B. He, J. He, L. Wang, X. Zhang, and E. Bi, "Effect of hydrogeological conditions and surface loads on shallow groundwater nitrate pollution in the Shaying River Basin: based on least squares surface fitting model," *Water Research*, vol. 163, article 114880, 2019.
- [6] R. Kumar, F. Heße, P. S. C. Rao et al., "Strong hydroclimatic controls on vulnerability to subsurface nitrate contamination across Europe," *Nature Communications*, vol. 11, no. 1, article 6302, 2020.
- [7] J. O. Lundberg, E. Weitzberg, and M. T. Gladwin, "The nitrate-nitrite-nitric oxide pathway in physiology and therapeutics," *Nature Reviews Drug Discovery*, vol. 7, no. 2, pp. 156–167, 2008.
- [8] S. Lidder and A. J. Webb, "Vascular effects of dietary nitrate (as found in green leafy vegetables and beetroot) via the nitrate-nitrite-nitric oxide pathway," *British Journal of Clinical Pharmacology*, vol. 75, no. 3, pp. 677–696, 2013.
- [9] A. Motevalli, S. A. Naghibi, H. Hashemi, R. Berndtsson, B. Pradhan, and V. Gholami, "Inverse method using boosted regression tree and k-nearest neighbor to quantify effects of point and non-point source nitrate pollution in groundwater," *Journal of Cleaner Production*, vol. 228, pp. 1248–1263, 2019.
- [10] D. Hao, C. Liu, X. Xu et al., "Surface defect-abundant one-dimensional graphitic carbon nitride nanorods boost photocatalytic nitrogen fixation," *New Journal of Chemistry*, vol. 44, no. 47, pp. 20651–20658, 2020.
- [11] Y. Y. Tong, H. Guo, D. Liu et al., "Vacancy engineering of iron-doped W₁₈O₄₉ nanoreactors for low-barrier electrochemical nitrogen reduction," *Angewandte Chemie-International Edition*, vol. 59, no. 19, pp. 7356–7361, 2020.
- [12] H. Kobayashi, A. Hayakawa, K. D. K. A. Somarathne, and E. C. Okafor, "Science and technology of ammonia combustion," *Proceedings of the Combustion Institute*, vol. 37, no. 1, pp. 109–133, 2019.
- [13] W. Wang, J. M. Herreros, A. Tsolakis, and A. P. E. York, "Ammonia as hydrogen carrier for transportation; investigation of the ammonia exhaust gas fuel reforming," *International Journal of Hydrogen Energy*, vol. 38, no. 23, pp. 9907–9917, 2013.
- [14] Y. Zhao, B. P. Setzler, J. Wang et al., "An efficient direct ammonia fuel cell for affordable carbon-neutral transportation," *Joule*, vol. 3, no. 10, pp. 2472–2484, 2019.
- [15] X. L. Xue, R. Chen, C. Yan et al., "Review on photocatalytic and electrocatalytic artificial nitrogen fixation for ammonia synthesis at mild conditions: advances, challenges and perspectives," *Nano Research*, vol. 12, no. 6, pp. 1229–1249, 2019.
- [16] Q. Hao, C. Liu, G. Jia et al., "Catalytic reduction of nitrogen to produce ammonia by bismuth-based catalysts: state of the art and future prospects," *Materials Horizons*, vol. 7, no. 4, pp. 1014–1029, 2020.
- [17] Y. Liu, B. Huang, X. Chen et al., "Electrocatalytic production of ammonia: biomimetic electrode-electrolyte design for efficient electrocatalytic nitrogen fixation under ambient conditions," *Applied Catalysis B-Environmental*, vol. 271, article 118919, 2020.
- [18] C. W. Liu, Q. Li, J. Zhang, Y. Jin, D. R. MacFarlane, and C. Sun, "Theoretical evaluation of possible 2D boron monolayer in N₂ electrochemical conversion into ammonia," *Journal of Physical Chemistry C*, vol. 122, no. 44, pp. 25268–25273, 2018.
- [19] C. W. Liu, Q. Li, C. Wu et al., "Single-boron catalysts for nitrogen reduction reaction," *Journal of the American Chemical Society*, vol. 141, no. 7, pp. 2884–2888, 2019.
- [20] S. Zhang, Y. Zhao, R. Shi, G. I. N. Waterhouse, and T. Zhang, "Photocatalytic ammonia synthesis: recent progress and future," *EnergyChem*, vol. 1, no. 2, article 100013, 2019.

- [21] W. H. Guo, K. Zhang, Z. Liang, R. Zou, and Q. Xu, "Electrochemical nitrogen fixation and utilization: theories, advanced catalyst materials and system design," *Chemical Society Reviews*, vol. 48, no. 24, pp. 5658–5716, 2019.
- [22] D. R. Hao, Y. Liu, S. Gao et al., "Emerging artificial nitrogen cycle processes through novel electrochemical and photochemical synthesis," *Materials Today*, vol. 46, pp. 212–233, 2021.
- [23] D. Hao, Z. G. Chen, M. Figliola, I. Stepniak, W. Wei, and B. J. Ni, "Emerging alternative for artificial ammonia synthesis through catalytic nitrate reduction," *Journal of Materials Science & Technology*, vol. 77, pp. 163–168, 2021.
- [24] Q. Hao, G. Jia, W. Wei et al., "Graphitic carbon nitride with different dimensionalities for energy and environmental applications," *Nano Research*, vol. 13, no. 1, pp. 18–37, 2020.
- [25] Q. Hao, C. Xie, Y. Huang et al., "Accelerated separation of photogenerated charge carriers and enhanced photocatalytic performance of g-C₃N₄ by Bi₂S₃ nanoparticles," *Chinese Journal of Catalysis*, vol. 41, no. 2, pp. 249–258, 2020.
- [26] Q. Huang, C. Wang, D. Hao, W. Wei, L. Wang, and B. J. Ni, "Ultralight biodegradable 3D-g-C₃N₄ aerogel for advanced oxidation water treatment driven by oxygen delivery channels and triphase interfaces," *Journal of Cleaner Production*, vol. 288, article 125091, 2020.
- [27] H. Zhang, Z. Liu, Y. Li et al., "Intimately coupled TiO₂/g-C₃N₄ photocatalysts and *in-situ* cultivated biofilms enhanced nitrate reduction in water," *Applied Surface Science*, vol. 503, article 144092, 2020.
- [28] J. Zhao, N. Li, R. Yu, Z. Zhao, and J. Nan, "Magnetic field enhanced denitrification in nitrate and ammonia contaminated water under 3D/2D Mn₂O₃/g-C₃N₄ photocatalysis," *Chemical Engineering Journal*, vol. 349, pp. 530–538, 2018.
- [29] X. Liu, H. Liu, Y. Wang, W. Yang, and Y. Yu, "Nitrogen-rich g-C₃N₄@AgPd Mott-Schottky heterojunction boosts photocatalytic hydrogen production from water and tandem reduction of NO₃⁻ and NO₂⁻," *Journal of Colloid and Interface Science*, vol. 581, Part B, pp. 619–626, 2020.
- [30] H. Hirakawa, M. Hashimoto, Y. Shiraiishi, and T. Hirai, "Selective nitrate-to-ammonia transformation on surface defects of titanium dioxide photocatalysts," *ACS Catalysis*, vol. 7, no. 5, pp. 3713–3720, 2017.
- [31] L. Cao, Q. Luo, J. Chen et al., "Dynamic oxygen adsorption on single-atomic ruthenium catalyst with high performance for acidic oxygen evolution reaction," *Nature Communications*, vol. 10, no. 1, article 4849, 2019.
- [32] K. Baek, W. C. Jeon, S. Woo et al., "Synergistic effect of quinary molten salts and ruthenium catalyst for high-power-density lithium-carbon dioxide cell," *Nature Communications*, vol. 11, no. 1, article 456, 2020.
- [33] T. T. Li, B. Shan, W. Xu, and T. J. Meyer, "Electrocatalytic CO₂ reduction with a ruthenium catalyst in solution and on nanocrystalline TiO₂," *ChemSusChem*, vol. 12, no. 11, pp. 2402–2408, 2019.
- [34] B. Lin, L. Heng, B. Fang et al., "Ammonia synthesis activity of alumina-supported ruthenium catalyst enhanced by alumina phase transformation," *ACS Catalysis*, vol. 9, no. 3, pp. 1635–1644, 2019.
- [35] S. Hennessey, P. Farràs, J. Benet-Buchholz, and A. Llobet, "A Bpp-based dinuclear ruthenium photocatalyst for visible light-driven oxidation reactions," *Catalysis Science & Technology*, vol. 9, no. 23, pp. 6760–6768, 2019.
- [36] M. Elcheikh Mahmoud, H. Audi, A. Assoud, T. H. Ghaddar, and M. Hmadeh, "Metal-organic framework photocatalyst incorporating bis(4'-(4-carboxyphenyl)-terpyridine)ruthenium(II) for visible-light-driven carbon dioxide reduction," *Journal of the American Chemical Society*, vol. 141, no. 17, pp. 7115–7121, 2019.
- [37] X. Li, X. Zhang, H. O. Everitt, and J. Liu, "Light-induced thermal gradients in ruthenium catalysts significantly enhance ammonia production," *Nano Letters*, vol. 19, no. 3, pp. 1706–1711, 2019.
- [38] G. Kresse and J. Furthmüller, "Efficiency of ab-initio total energy calculations for metals and semiconductors using a plane-wave basis set," *Computational Materials Science*, vol. 6, no. 1, pp. 15–50, 1996.
- [39] G. Kresse and J. Hafner, "Ab initio molecular dynamics for liquid metals," *Physical Review B*, vol. 47, no. 1, article 558, 561 pages, 1993.
- [40] G. Kresse, J. Furthmüller, and J. Hafner, "Theory of the crystal structures of selenium and tellurium: the effect of generalized-gradient corrections to the local-density approximation," *Physical Review B*, vol. 50, no. 18, article 13181, 13185 pages, 1994.
- [41] G. Kresse and J. Furthmüller, "Efficient iterative schemes for ab initio total-energy calculations using a plane-wave basis set," *Physical Review B*, vol. 54, no. 16, article 11169, 11186 pages, 1996.
- [42] Q. Hao, S. Hao, X. Niu, X. Li, D. Chen, and H. Ding, "Enhanced photochemical oxidation ability of carbon nitride by π - π stacking interactions with graphene," *Chinese Journal of Catalysis*, vol. 38, no. 2, pp. 278–286, 2017.
- [43] M. Kehler, J. Duchoslav, A. Hinterreiter et al., "XPS investigation on the reactivity of surface imine groups with TFAA," *Plasma Processes and Polymers*, vol. 16, no. 4, article 1800160, 2019.
- [44] A. Khaniya, S. Ezzat, Q. Cumston, K. R. Coffey, and W. E. Kaden, "Ru(0001) and SiO₂/Ru(0001): XPS study," *Surface Science Spectra*, vol. 27, no. 2, article 024009, 2020.
- [45] H. Lu, Q. Hao, T. Chen et al., "A high-performance Bi₂O₃/Bi₂-SiO₅ p-n heterojunction photocatalyst induced by phase transition of Bi₂O₃," *Applied Catalysis B-Environmental*, vol. 237, pp. 59–67, 2018.
- [46] H. Kominami, A. Furusho, S. Y. Murakami, H. Inoue, and Y. Kera, "Effective photocatalytic reduction of nitrate to ammonia in an aqueous suspension of metal-loaded titanium (IV) oxide particles in the presence of oxalic acid," *Catalysis Letters*, vol. 76, no. 1/2, pp. 31–34, 2001.
- [47] Y. Wang, Y. Tian, L. Yan, and Z. Su, "DFT study on sulfur-doped g-C₃N₄ nanosheets as a photocatalyst for CO₂ reduction reaction," *The Journal of Physical Chemistry C*, vol. 122, no. 14, pp. 7712–7719, 2018.
- [48] Q. Hao, X. Niu, C. Nie et al., "A highly efficient g-C₃N₄/SiO₂ heterojunction: the role of SiO₂ in the enhancement of visible light photocatalytic activity," *Physical Chemistry Chemical Physics*, vol. 18, no. 46, pp. 31410–31418, 2016.
- [49] Y. du, Q. Hao, D. Chen et al., "Facile fabrication of heterostructured bismuth titanate nanocomposites: the effects of composition and band gap structure on the photocatalytic activity performance," *Catalysis Today*, vol. 297, pp. 255–263, 2017.
- [50] G. R. Beecher, B. A. Warden, and H. Merken, "Analysis of tea polyphenols," *Proceedings of the Society for Experimental Biology and Medicine*, vol. 220, no. 4, pp. 267–270, 1999.

- [51] M. Chrysochoou, J. Oakes, and M. D. Dyar, "Investigation of iron reduction by green tea polyphenols," *Applied Geochemistry*, vol. 97, pp. 263–269, 2018.
- [52] J. S. Oakes, *Investigation of iron Reduction by Green Tea Polyphenols for Application in Soil Remediation*, 2013.
- [53] P. Vanýsek, "Electrochemical series," *Handbook of Chemistry and Physics*, vol. 93, pp. 5–80, 2012.